Magnetotransport in Aharonov-Bohm interferometers: Exact numerical simulations

Salil Bedkihal and Dvira Segal

Chemical Physics Theory Group, Department of Chemistry, University of Toronto, 80 Saint George Street, Toronto, Ontario, Canada M5S 3H6

(Received 21 July 2014; revised manuscript received 5 October 2014; published 3 December 2014)

The linear conductance of a two-terminal Aharonov-Bohm interferometer is an even function of the applied magnetic flux, as dictated by the Onsager-Casimir symmetry. Away from linear response this symmetry may be broken when many-body interactions are in effect. Using a numerically exact simulation tool, we study the dynamics and the steady-state behavior of the out-of-equilibrium double-dot Aharonov-Bohm interferometer, while considering different types of interactions: Model I includes a closed interferometer with an interdot electron-electron repulsion energy. In model II the interferometer is interacting with a dissipative environment, possibly driven away from equilibrium. In both cases we show that depending on the (horizontal, vertical) mirror symmetries of the setup, nonlinear transport coefficients obey certain magnetosymmetries. We compare numerically exact simulations to phenomenological approaches and special limits: The behavior of model I is compared to self-consistent mean-field calculations and master equation results in the Coulomb blockade regime. Model II, allowing heat dissipation to a thermal bath, is mimicked by an Aharonov-Bohm junction with a voltage probe. In both cases we find that phenomenological treatments capture the relevant transport symmetries, yet significant deviations in magnitude may show up.

DOI: 10.1103/PhysRevB.90.235411 PACS number(s): 73.23.−b, 03.65.Yz, 73.63.Kv

I. INTRODUCTION

Microreversibility dictates linear response properties such as the Onsager-Casimir symmetry relations. Particularly, in a two-terminal conductor the linear conductance should be an even function of the magnetic field B [1]. In Aharonov-Bohm (AB) interferometers, this symmetry is displayed by the "phase rigidity" of the conductance oscillations with B [2,3]. Microreversibility is broken beyond linear response; thus magnetoasymmetries should develop at finite bias, as demonstrated in several experiments [4–11]. What is then remarkable is not the failure of the Onsager symmetry away from equilibrium, rather the development of more general symmetries between nonlinear transport coefficients and high-order cumulants [12–15].

Several studies explored magnetotransport in AB interferometers beyond the noninteracting limit, coupling electrons to either internal or external degrees of freedom [16–21]. For example, the problem has been explored by implementing mean-field arguments within scattering theories, focusing on effective quantities such as the screening potential developing in the interferometer in response to an external bias [13,16]. At this level, one can show that magnetoasymmetries develop since internal potentials (the result of many-body interactions) are asymmetric in the magnetic field away from equilibrium [13,16]. In the complementary (phenomenological) Büttiker probes approach [22] elastic and inelastic scattering effects are introduced via probes whose parameters reflect the response of the conductor to the applied magnetic field and the voltage bias [23]. Beyond phenomenological treatments, magnetotransport characteristics were investigated using microscopic models in the Coulomb blockade limit [19,21] and in the Kondo regime [19].

In this work we study characteristics of nonlinear transport in AB interferometers by means of an exact numerical technique [24]. Our setup includes an AB interferometer with two quantum dots, one at each arm, and we introduce different types of many-body effects within the system: Model I includes an interdot Coulombic repulsion term; see Fig. 1. In model II a secondary fermionic environment interacts capacitively with one of the quantum dots. This environment can serve as a "charge sensor" or a "quantum point contact"; see Fig. 2. We simulate the dynamics and the steady-state properties of these (many-body out-of-equilibrium) setups by adapting an iterative influence functional path integral technique (INFPI), developed in Ref. [24] to treat the dynamics of the single-impurity Anderson dot model.

Our work includes the following contributions: (i) We study symmetries of magnetotransport far from equilibrium in the transient domain and in the steady-state limit including *genuine* many-body interactions, rather than using phenomenological (screening, probe) models [13,16]. (ii) Magnetotransport characteristics were explored in the literature within different models, e.g., considering an interferometer made with one or two quantum dots, with or without thermal dissipation effects. Here, we study transport symmetries in different models using the same computational tool, allowing for a direct comparison. (iii) We compare exact simulations to phenomenological treatments and limit cases (e.g., Coulomb blockade results), for clarifying the validity and accuracy of approximate techniques in magnetotransport calculations, and the relevance of special-extreme limit situations. Particularly, in model II our simulations reveal functionalities beyond the mean-field level: diode (dc-rectification) effect at zero flux under spatial asymmetry and a finite Coulomb drag current, driven by the fermionic environment.

The paper is organized as follows. In Sec. II we introduce two models of an interacting double-dot interferometer, and the principles of the numerical techniques adopted in this work. Results are presented in Sec. III. Section IV concludes. For simplicity, we set $e = 1$, $\hbar = 1$, and $k_B = 1$.

II. MODELS AND TECHNIQUES

A. Double-dot AB interferometer

We begin with the noninteracting Hamiltonian, common to the two models. It includes a two-terminal ($\nu = L, R$) AB

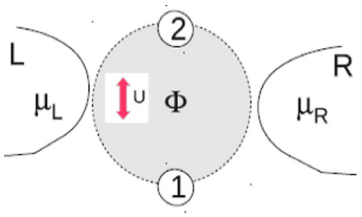

FIG. 1. (Color online) Scheme of model I, a two-terminal double-dot Aharonov-Bohm interferometer with spinless electrons in two quantum dots, 1 and 2, with an interdot repulsion of strength U.

interferometer with two dots, $n = 1,2$, one at each arm. For simplicity, we ignore the spin degree of freedom, and take into account only one electronic level in each dot. The Hamiltonian includes the following terms:

$$H_{AB} = \sum_{n=1,2} \epsilon_n a_n^\dagger a_n + \sum_{l\in L} \epsilon_l a_l^\dagger a_l + \sum_{r\in R} \epsilon_r a_r^\dagger a_r + \sum_{n=1,2}\sum_{l\in L} v_{n,l} a_n^\dagger a_l e^{i\phi_n^L} + \sum_{n=1,2}\sum_{r\in R} v_{n,r} a_r^\dagger a_n e^{i\phi_n^R} + \text{H.c.} \quad (1)$$

Here $a_k^\dagger$ (a_k) are fermionic creation (annihilation) operators of electrons with momentum k and energy ϵ_k in the $k \in \nu$ metal, $a_n^\dagger$ and a_n are the respective operators for electrons on the dots, and ϵ_n denotes the energy of spin-degenerate levels. The parameter $v_{n,l}$ stands for the coupling strength of dot n to the l state of the L metal. A similar definition holds for $v_{n,r}$. These coupling terms are absorbed into the definition of the hybridization energy

$$\gamma_{\nu,n}(\epsilon) = 2\pi \sum_{j\in\nu} |v_{n,j}|^2 \delta(\epsilon - \epsilon_j). \quad (2)$$

In our simulations we set $\gamma_{\nu,n}$, use a constant density of states for the metals, up to a sharp cutoff $\pm D$, then construct the real-valued tunneling elements $v_{n,j}$ by using Eq. (2). The AB phase factors ϕ_n^L and ϕ_n^R are acquired by electrons in a magnetic field perpendicular to the device plane. These phases are constrained to satisfy

$$\phi_1^L - \phi_2^L + \phi_1^R - \phi_2^R = \phi = 2\pi\Phi/\Phi_0, \quad (3)$$

and we adopt the gauge

$$\phi_1^L - \phi_2^L = \phi_1^R - \phi_2^R = \phi/2. \quad (4)$$

Here Φ is the magnetic flux threading through the AB ring, $\phi = 2\pi\Phi/\Phi_0$ the magnetic phase, and $\Phi_0 = h/e$ the magnetic flux quantum. We voltage-bias the AB interferometer, $\Delta\mu \equiv \mu_L - \mu_R$, with $\mu_{L,R}$ as the chemical potential of the metals; we use the convention of a positive current flowing left-to-right. We bias the system in a symmetric manner, $\mu_L = -\mu_R$, but this choice does not limit the generality of our discussion since the dots may be gated away from the so called "symmetric point" at which $\mu_L - \epsilon_n = \epsilon_n - \mu_R$.

The Hamiltonian (1) does not include interactions and one can readily obtain the exact form of the (steady-state) charge current flowing between the terminals, an even function of the magnetic flux [23]. Assuming for simplicity that the two quantum dots are evenly coupled to the ν terminal, $\gamma_\nu \equiv \gamma_{\nu,n}$, we find that [25]

$$I(\phi) = \frac{1}{2\pi}\int_{-\infty}^{\infty} d\epsilon \frac{4\gamma_L\gamma_R\left[(\epsilon-\epsilon_d)^2\cos^2\frac{\phi}{2} + \left(\frac{\Delta\epsilon}{2}\sin\frac{\phi}{2}\right)^2\right][f_L(\epsilon) - f_R(\epsilon)]}{\left[(\epsilon-\epsilon_d)^2 - \frac{\Delta\epsilon^2}{4} - \gamma_L\gamma_R\sin^2\frac{\phi}{2}\right]^2 + (\gamma_L+\gamma_R)^2(\epsilon-\epsilon_d)^2}, \quad (5)$$

with $\epsilon_d = (\epsilon_1 + \epsilon_2)/2$ and $\Delta\epsilon = \epsilon_1 - \epsilon_2$. Here $f_\nu(\epsilon) = [e^{\beta(\epsilon-\mu_\nu)} + 1]^{-1}$ with $\beta = 1/T$ as the inverse temperature. The current is an even function in the magnetic flux at finite bias, irrespective of spatial asymmetries ($\gamma_L \neq \gamma_R$ and $\Delta\epsilon \neq 0$). Using the probe technique, a phenomenological tool for implementing scattering effects, we had recently proved that this "phase locking" behavior is preserved under elastic dephasing [23]. In contrast, inelastic scattering processes, taken into account with a voltage probe or a voltage-temperature probe, break the even symmetry in ϕ in the nonlinear transport regime. We now augment the Hamiltonian (1) with genuine many-body interactions: In model I we add an interdot repulsion interaction between electrons, overall conserving energy and charge in the interferometer. In model II energy exchange with an additional environment is allowed.

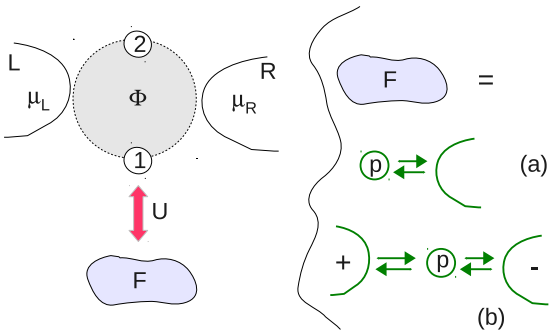

FIG. 2. (Color online) Scheme of model II, a two-terminal double-dot Aharonov-Bohm interferometer coupled to a fermionic environment. This environment consists of a quantum dot (labeled p) itself hybridized with either (a) an equilibrium sea of noninteracting electrons, or (b) two metals ($\pm$), possibly biased away from equilibrium. In both cases dot 1 of the interferometer is coupled capacitively (strength U) to dot p in the fermionic environment.

1. Model I: Interdot Coulomb repulsion

We complement the Hamiltonian (1) with a Coulomb repulsion term, nonzero when both quantum dots are occupied. The resulting interdot Coulomb (C) model reads

$$H_C = H_{AB} + U n_1 n_2. \quad (6)$$

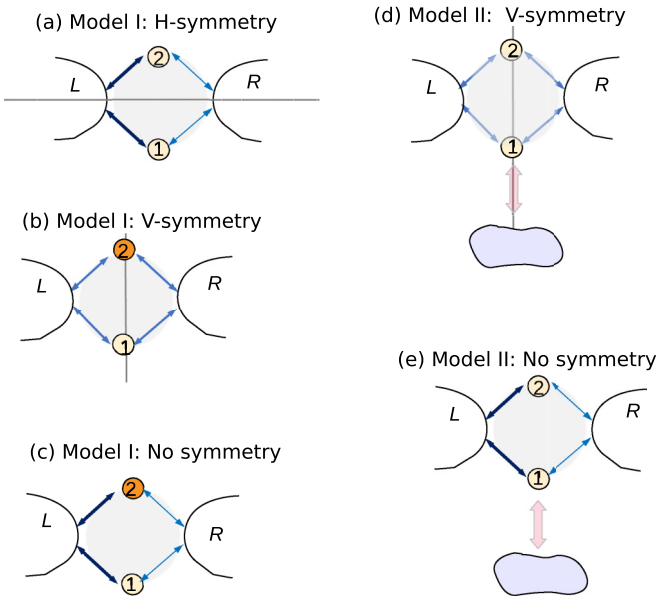

FIG. 3. (Color online) Schemes of the different setups considered in this work. (a) Model I with a horizontal (H) mirror symmetry. The bold (light) arrows represent strong (weak) hybridization energies of the quantum dots to the metals. Simulations are included in Fig. 4. (b) Model I with a vertical (V) mirror symmetry. The nondegenerate dots are represented by different colors. Figure 5 displays the transients; Fig. 8 shows steady-state values. (c) Model I missing the H and V mirror symmetries; see data in Figs. 7 and 8. (d) Model II with a V mirror symmetry. Results are displayed in Figs. 11 and 13. (e) Model II missing both the H and V mirror symmetries. Steady-state data are included in Fig. 13.

For a schematic representation see Fig. 1. Here $n_1 = a_1^\dagger a_1$ and $n_2 = a_2^\dagger a_2$ are the number operators for the dots. The behavior of the current and the occupation of the dots in this "interacting two-level quantum dot model" were investigated in different works: The case without the threading magnetic field was studied, e.g., in Refs. [26–29]. The role of an external magnetic field was examined in different limits, particularly in the Coulomb blockade regime [30]. Recent studies further investigated transient effects, either analytically, disregarding interactions [31], or numerically, considering relatively weak interactions [32].

In our simulations below we consider three geometries for model I (see Fig. 3): (i) a setup with a mirror symmetry with respect to the horizontal axis, (ii) the case with a mirror symmetry along the vertical axis, and (iii) the model missing (horizontal and vertical) symmetries.

2. *Model II: Coupling to a fermionic environment*

Dissipation effects can be included by capacitively coupling the interferometer to a fermionic environment (FE), set in equilibrium or out of equilibrium. For simplicity, we do not consider electron-electron interactions within the interferometer or within the FE. This dissipative (D) Hamiltonian includes the interferometer [Eq. (1)], an additional FE, and the interaction energy between the units,

$$H_D = H_{AB} + H_F + V_D. \tag{7}$$

The FE is realized here by a tunneling junction

$$H_F = \epsilon_p c_p^\dagger c_p + \sum_{s\in\alpha} \epsilon_s c_s^\dagger c_s + \sum_{s\in\alpha} g_s c_s^\dagger c_p + \text{H.c.} \tag{8}$$

It includes a quantum dot of energy ϵ_p coupled to two reservoirs ($\alpha = \pm$). The FE may be set at equilibrium when $\mu_+ = \mu_-$ (with the Fermi energy set at zero), or biased away from equilibrium, $\Delta\mu_F \equiv \mu_+ - \mu_- \neq 0$. We distinguish between the AB interferometer and the FE by adopting the operators $c^\dagger$ and c to denote creation and annihilation operators of electrons in the FE. We define the dot-reservoir hybridization energies in the FE by

$$\gamma_\alpha(\epsilon) = 2\pi \sum_{s\in\alpha} |g_s|^2 \delta(\epsilon - \epsilon_s). \tag{9}$$

Electrons in the AB interferometer and the FE are interacting (strength U) according to the form

$$V_D = U n_p n_1. \tag{10}$$

Here $n_p = c_p^\dagger c_p$, $n_1 = a_1^\dagger a_1$ are number operators. Note that there is no leakage of electrons from the AB junction into the FE. However, this additional environment provides a mechanism for inducing elastic and inelastic scattering events of electrons on dot 1.

Model II has been examined in the literature in the context of charge sensing, and as a "which-path" detector; see for example Refs. [33–35]. The dephasing in an AB interferometer with a capacitively coupled charge sensor has been analyzed in Ref. [33], using a second-order perturbation theory in U, yet limited to the linear conductance case. Here, using a numerical tool, we analyze the system away from equilibrium with the vertical mirror symmetry either preserved or violated; see Fig. 3.

B. Observables

The principal observable of interest in our work is the charge current in the interferometer. It is calculated from the current operator,

$$\begin{aligned}\hat{I}_L &= -\frac{dN_L}{dt} = -i[H, N_L] \\ &= \sum_{l\in L} \left[-i v_{1,l} e^{i\phi_1^L} a_1^\dagger a_l + i v_{l,1} e^{-i\phi_1^L} a_l^\dagger a_1\right],\end{aligned} \tag{11}$$

with $N_L = \sum_{l\in L} a_l^\dagger a_l$ as the number operator of the L metal. The current at the R contact, $\hat{I}_R$, can be defined in a analogous way. We identify the averaged current by $\hat{I} \equiv \frac{1}{2}(\hat{I}_L - \hat{I}_R)$; we could simulate separately the currents at the L and R terminals, but we chose to directly compute the expectation value

$$I(t,\phi) = \text{tr}[\rho(0) e^{iHt} \hat{I} e^{-iHt}], \tag{12}$$

from a dot-metal-FE factorized initial state $\rho(0)$. Here H denotes the total Hamiltonian of interest. Formally, the two-terminal current $I(t,\phi)$ can be expanded in powers of the applied voltage bias $\Delta\mu$,

$$I(t,\phi) = \sum_{k=1,2,..} G_k(t,\phi)(\Delta\mu)^k. \tag{13}$$

We refer to $G_{k>1}$ as nonlinear conductance coefficients. The current can be separated into its odd and even terms in powers of the bias. Even terms represent the dc-rectification contribution,

$$\mathcal{R}(t,\phi) \equiv \tfrac{1}{2}[I(t,\phi) + \bar{I}(t,\phi)] = G_2(t,\phi)(\Delta\mu)^2 + G_4(t,\phi)(\Delta\mu)^4 + \cdots . \quad (14)$$

Here $\bar{I}$ is the current obtained when interchanging the chemical potentials of the two terminals (assuming identical temperatures). The complementary odd terms are grouped into

$$\mathcal{D}(t,\phi) \equiv \tfrac{1}{2}[I(t,\phi) - \bar{I}(t,\phi)] = G_1(t,\phi)\Delta\mu + G_3(t,\phi)(\Delta\mu)^3 + \cdots . \quad (15)$$

Below we relax the time variable when addressing long-time quasi-steady-state values. Other quantities of interest are the occupation of the dots in the interferometer and the behavior of the coherences, off-diagonal terms of the reduced density matrix, obtained from $\sigma_{n,n'}(t) \equiv \mathrm{tr}_{\mathrm{e}}[e^{-iHt}\rho(0)e^{iHt}]_{n,n'}$; the trace is performed over degrees of freedom in the electronic reservoirs. We could also simulate the dynamics within the FE (model II), exploring its operation as a quantum point contact and a magnetic field sensor.

It should be noted that, by definition, a nonzero value for $\mathcal{R}$ reveals deviations from linear response. In contrast, as we show below in our simulations, within the range of parameters adopted here $\mathcal{D}$ is still dominated by the linear response term, satisfying the Onsager symmetry. Practically, we obtain $\mathcal{R}$ ($\mathcal{D}$) by simulating the current in the forward and reversed bias configurations, then adding (subtracting) the resulting currents.

Focusing on the current in the AB unit, we consider different setups for models I and II; see Fig. 3. From symmetry considerations, under a mirror symmetry with respect to the horizontal (H) axis, phase locking should take place, with $I(\phi) = I(-\phi)$ [30]. On the other hand, if the system acquires only a mirror symmetry with respect to the vertical (V) axis, the resulting symmetry relation is $I(\phi) = -\bar{I}(-\phi)$ [30], leading to

$$\mathcal{R}(\phi) = -\mathcal{R}(-\phi), \quad \mathcal{D}(\phi) = \mathcal{D}(-\phi). \quad (16)$$

Below, our numerical results confirm these relations in the transient domain as well, under a symmetrized definition of the current operator, with a symmetric application of bias ($\mu_L = -\mu_R$). We quantify the importance of $\mathcal{R}$ relative to $\mathcal{D}$, study deviations from the above relations when the vertical and horizontal symmetries are broken, and test predictions of approximate techniques against exact simulations.

C. Numerically exact treatment: INFPI

We simulate the dynamics of electrons in models I and II using a numerically exact influence function path integral technique, referred to as INFPI. The principles of this method have been detailed in several recent publications [24,26,36]; therefore we only highlight here the aspects of relevance to the present work.

Equations (6) and (7) can be each organized into the generic form $H = H_0 + H_1$, with H_0 comprising the exactly solvable (noninteracting) terms. Many-body interactions are collected into H_1, written in the form

$$H_1 = U\left[n_1 n_a - \tfrac{1}{2}(n_1 + n_a)\right]. \quad (17)$$

In model I, $n_a = n_2$; in model II it corresponds to the number operator of the impurity level p within the FE, $n_a = n_p = c_p^\dagger c_p$ [see Eq. (10)]. The two-body term $\frac{1}{2}U(n_1 + n_a)$ is absorbed into the definition of H_0. This structure allows for the elimination of H_1 via the Hubbard-Stratonovich (HS) transformation and the propagation of quadratic expectation values with an influence functional path integral technique. We now briefly review the principles of INFPI, to explain why this method is fitting for the study of magnetotransport in far-from-equilibrium situations. We discuss the numerical errors associated with INFPI simulations, and point out that these errors do not interfere with the resolution of transport symmetries.

The starting point in our approach is the formal expression (12). As an initial condition we use a factorized initial state. For example, in model II we use $\rho(0) = \rho_F(0) \otimes \rho_{AB}(0)$ with ρ_{AB} as the state of the interferometer. We further assume that $\rho_{AB}(0) = \sigma(0) \otimes \rho_L \otimes \rho_R$, with $\sigma(0)$ as the reduced density matrix of the isolated dots in the interferometer. The FE is similarly prepared in a factorized state with $\rho_F(0) = \rho_p(0) \otimes \rho_+ \otimes \rho_-$. The four reservoirs $\xi = L, R, \pm$ are separately prepared in grand canonical states at a given chemical potential and temperature, $\rho_\xi = e^{-\beta(H_\xi - \mu_\xi N_\xi)}/\mathrm{tr}[e^{-\beta(H_\xi - \mu_\xi N_\xi)}]$; we prepare all reservoirs at the same temperature $1/\beta$.

Using this initial state in Eq. (12), we apply the Trotter decomposition and the HS transformation; the latter eliminates the many-body term H_1 by introducing auxiliary Ising variables [37]. The result is a formally exact path integral expression; the integrand is refereed to as the "influence functional" (IF) involving nonlocal dynamical correlations, generally missing an analytical form.

The fundamental principle behind INFPI is the observation that at finite temperature and/or nonzero chemical potential difference bath correlations exponentially decay in time; thus the IF can be truncated beyond a memory time τ_c [38,39]. This allows us to define an auxiliary operator on the time window τ_c, which can be time-evolved iteratively from the initial condition to time t. The truncated IF can be evaluated numerically by discretizing the fermionic reservoirs and tracing out the baths' degrees of freedom using trace identities [24].

The INFPI method involves three numerical errors: (i) The finite discretization of the reservoirs, each comprising L_s single-electron states. (ii) The time step adopted in the Trotter breakup, δt. In our simulations the trotter error grows as $(\delta t U)^2$. (iii) The error associated with the truncation of the IF, to include only a finite memory time τ_c. The exact limit is reached when $L_s \to \infty$, $U\delta t \to 0$, and $\tau_c \to t$. Convergence is tested by studying the sensitivity of simulations to the energy discretization of the reservoirs, the time step, and the memory time $\tau_c = N_s \delta t$, with N_s as an integer.

INFPI excellently fits for the simulation of magneto-transport in far-from-equilibrium situations: First, analytic considerations and numerical simulations suggest that the memory time characterizing the bath decorrelation process scales as $\tau_c \sim 1/\Delta\mu$ [24,38,39]. Thus, the method should quickly converge to the exact limit at a large bias. Since

we are specifically interested here in beyond-linear-response situations, INFPI is perfectly suited for the problem. Second, this is a deterministic time propagation scheme. Thus, it is an advantageous tool for testing magnetic field symmetries in nonlinear transport: Even if convergence is incomplete, $I(t,\phi)$ and $I(t,-\phi)$ deviate from the exact limit in the same (deterministic) form, conserving transport symmetries. In contrast, methods that rely on stochastic sampling of diagrams may accumulate distinct errors in the evaluation of the current at opposite phases, $I(t,\pm\phi)$; thus one may need to approach the exact limit for validating transport symmetries. As we show below, at finite interactions the evolution of the current with time strongly depends on the magnetic phase, showing distinct relaxation times for $\pm\phi$. Thus, it is important to adopt here techniques which accumulate identical errors for $\pm\phi$. Finally, INFPI is a flexible tool and it can be easily adapted for the study of several related models, as long as the interacting contribution H_1 follows Eq. (17). This allows us to analyze and compare the behavior of different many-body situations, e.g., with or without a dissipative bath.

D. Phenomenological approaches

Nonlinear transport characteristics in models I and II can be explored based on perturbation theory expansions in U; see for example Ref. [33]. Alternatively, in mean-field (MF) approaches many-body effects are embedded in the (noninteracting) scattering formalism. For example, one can write the scattering matrix as a functional of an electrostatic screening potential which depends on the applied bias [16,18]. Another phenomenological scheme has been explored in Ref. [23]: Buttiker's probes were used to apply different processes (elastic, inelastic, dissipative) into the otherwise coherent dynamics.

In Sec. III we compare results from INFPI to phenomenological methods. Model I is analyzed in the steady-state limit using the self-consistent Hartree approximation as described in Refs. [27,40,41]. This scheme accounts for the interdot Coulomb interaction by replacing the bare levels with Hartree energies, e.g., $\epsilon_1 \to \epsilon_1 + U\sigma_{2,2}$. We then use standard Green's function expressions [25], iterated to reach self-consistency. To understand the behavior of high-order conductance terms, we further compare our results to Bloch-type master equations valid in the large bias Coulomb blockade case.

We analyze model II using the phenomenological voltage probe technique, extended to the nonequilibrium regime, as explained in Ref. [23]. In this approach we hybridize the quantum dot 1 to a metal terminal (probe), then impose the condition of zero net charge current in this connection. Electrons can thus dephase and exchange energy in the probe, but (net) charge current only flows between the L and R terminals.

III. RESULTS

In our simulations below we adopt the following parameters: $\Delta\mu = 0.6$, inverse temperature of the electronic reservoirs $\beta = 50$, $U = 0.1$, $\gamma_{v,n} = 0.05$–0.2, flat bands extending between $D = \pm 1$. INFPI numerical parameters are $\delta t = 0.5$–1.2, $N_s = 3$–6, and $L_s = 120$. Convergence was reached for $\tau_c \sim 2$, in agreement with the rough estimate $\tau_c \sim 1/\Delta\mu$. We consider different setups, obeying or violating the horizontal and vertical mirror symmetries; see Fig. 3.

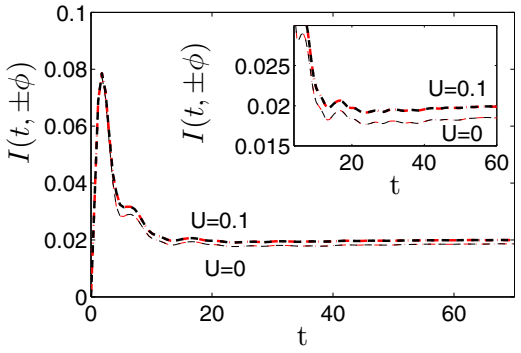

FIG. 4. (Color online) Model I with a horizontal mirror symmetry, showing phase rigidity. INFPI simulations using $\phi = \pm\pi/2$, $\gamma_{L,1} = \gamma_{L,2} = 0.2$, $\gamma_{R,1} = \gamma_{R,2} = 0.05$, $\epsilon_1 = \epsilon_2 = 0.15$, $\Delta\mu = 0.6$, $U = 0$ (bottom two overlapping lines) and $U = 0.1$ (top two overlapping lines) $N_s = 6$ and $\delta t = 0.6$. The inset zooms on the time evolution after the early transients.

A. Model I

We analyze nonlinear transport behavior in model I using INFPI simulations, then compare our results to the Hartree mean-field approach and the Coulomb blockade case. We begin with a setup preserving the horizontal symmetry, $\epsilon_1 = \epsilon_2$, $\gamma_{L,1} = \gamma_{L,2} > \gamma_{R,1} = \gamma_{R,2}$. As pointed out in Ref. [30], the current in this model should be an even function of the magnetic field, beyond linear response. Figure 4 confirms this "phase locking" behavior in the transient regime as well, given the symmetric initial condition and the symmetrized definition of the current operator.

In Fig. 5 we consider a setup with only a vertical mirror symmetry. We separate the current into its odd and even conductance terms by studying the dynamics with a reversed bias, then calculating $\mathcal{R} = (I + \bar{I})/2$ and $\mathcal{D} = (I - \bar{I})/2$. Using INFPI, we find that Eq. (16) is obeyed even before steady state is reached.

We exemplify the convergence behavior of this model in Fig. 6. In panels (a) and (b) we display $\mathcal{R}(t,\pm\pi/2)$ and demonstrate that it obeys the symmetry relation (16) even before convergence is achieved. We also examine the steady-state behavior of the system using different values for the simulation time step; see panels (c) and (d). A large time step $\delta t = 1.2$ does not allow convergence for $\mathcal{R}$, but with $\delta t = 0.6$, $\mathcal{R}(\pm\pi/2)$ converges around $\tau_c = 3$. Odd conductance terms [panel (d)] slowly converge, but again maintain transport symmetries [overlapping data for $\mathcal{D}(\pm\phi/2)$] under a short memory time. This observation is not trivial: the dynamics under the phases $\pm\phi$ is quite different, see for example Fig. 5(a). The fact that $\delta t = 1.2$ data seem to properly behave for $\mathcal{D}$, yet not for $\mathcal{R}$, should not be alarming: We found in previous studies that (within the same INFPI computation) different observables converge following different curves, with distinctive time step and memory time [26]. Since $\mathcal{R}$ and $\mathcal{D}$ conductance terms contain complementing scattering processes, it is not surprising that they follow different

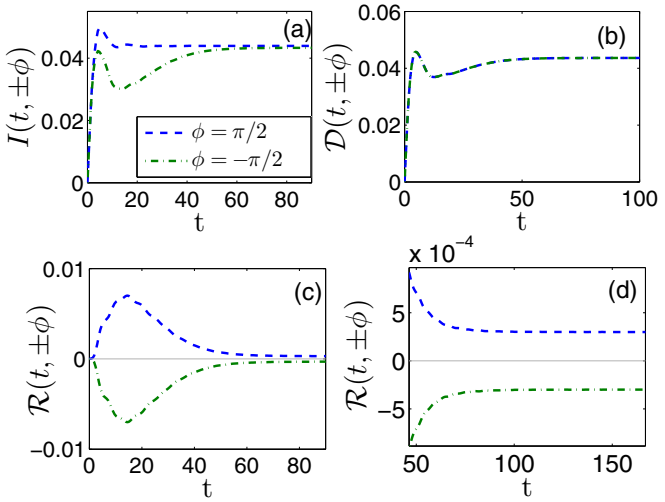

FIG. 5. (Color online) Model I with a vertical mirror symmetry. (a) Total current and its breakup into (b) $\mathcal{D}$ and (c)–(d) $\mathcal{R}$ components; $\phi = \pi/2$, $\gamma_{v,n} = 0.1$, $\epsilon_1 = 0.1$, $\epsilon_2 = 0.2$, $\Delta\mu = 0.6$, $U = 0.1$, $N_s = 6$, and $\delta t = 0.6$.

convergence patterns. We note that the $\mathcal{D}$ curve is reaching convergence with increasing τ_c; our interpretation of the $\mathcal{R}$ curve goes as follows: Results are meaningful as long as they are independent of the time step δt, when the Trotter error is

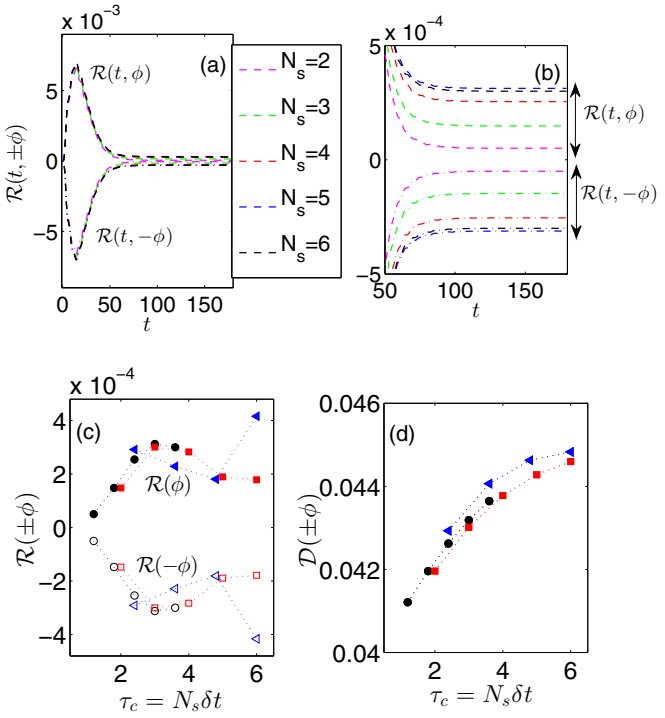

FIG. 6. (Color online) Example of a convergence analysis for model I with a vertical mirror symmetry using the data of Fig. 5. (a) and (b) $\mathcal{R}(t, \pm\pi/2)$ with $\delta t = 0.6$ and $N_s = 2,3,...,6$. Panel (b) zooms on the long-time behavior. (c) and (d) Long-time ($t \sim 180$) quasi-steady-state values of $\mathcal{R}(\pm\pi/2)$ and $\mathcal{D}(\pm\pi/2)$ as a function of $\tau_c = N_s \delta t$ for different time steps, $\delta t = 0.6$ (○), $\delta t = 1$ (□), and $\delta t = 1.2$ (triangle). Filled (empty) symbols stand for the $\phi = \pi/2$ ($\phi = -\pi/2$) magnetic phases, overlapping in panel (d).

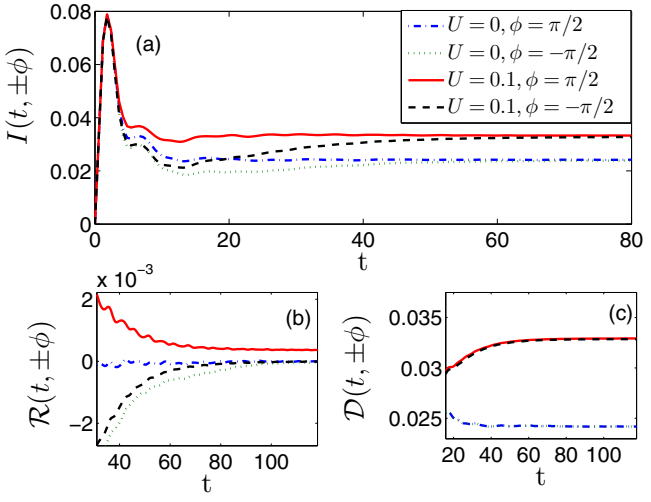

FIG. 7. (Color online) Model I. (a) Total current and its breakup into its (b) $\mathcal{R}$ and (c) $\mathcal{D}$ components for noncentrosymmetric and nondegenerate double-dot system; $\phi = \pi/2$, $\gamma_{L,1} = \gamma_{L,2} = 0.2$, $\gamma_{R,1} = \gamma_{R,2} = 0.05$, $\epsilon_1 = 0.1$, $\epsilon_2 = 0.2$, $\Delta\mu = 0.6$, $U = 0.1$, $N_s = 6$, and $\delta t = 0.6$.

insignificant. At small τ_c, its increase through N_s directs us to convergence. However, as we increase N_s we add time evolution operators and collect a larger total Trotter error, deviating us from the exact answer, though τ_c is increasing. This is reflected by the departure from the (short) plateau around $\tau_c \sim 3$–4 in Fig. 6(c). Thus, to reach convergence one should simultaneously increase N_s and reduce δt, to make sure no significant errors are accumulated due to either source. Following this discussion, we take below the values obtained with the smallest time step, $\delta t = 0.6$ and $N_s = 6$ to represent INFPI's numerical solution here. More extensive simulations, with $\delta t \sim 0.5$ and $N_s = 2$–10, are necessary to achieve more accurate values for $\mathcal{R}$.

The symmetry relations (16) are invalidated when the horizontal and vertical mirror symmetries are broken; see Fig. 7. Note that in panel (c), $\mathcal{D}(\phi) \neq \mathcal{D}(-\phi)$; deviations are order of 10^{-4}. We can use Fig. 7 and estimate the magnitude of high-order conductances. For example, from the behavior of $\mathcal{D}$ (assuming G_3 provides the largest contribution after G_1) we find that at $\phi = \pi/2$, $G_1 \sim \mathcal{D}/\Delta\mu = 0.06$, $G_3 \sim [\mathcal{D}(\pi/2) - \mathcal{D}(-\pi/2)]/2\Delta\mu^3 \sim 5 \times 10^{-4}$, and $G_2(\pi/2) \sim R(\pi/2)/\Delta\mu^2 \sim 10^{-3}$. Thus, at this phase, $G_3/G_1 = 10^{-2}$ and $G_2/G_1 = 2 \times 10^{-2}$. These conductances are translated to physical units when multiplied by the factor $\frac{2e^2}{\hbar}$. Note that G_2 and G_3 are of the same order of magnitude.

In Fig. 8 we display the long-time quasi-steady-state data for $\mathcal{R}(\phi)$ and $\mathcal{D}(\phi)$. Within the present simulation times, we have not reached the steady-state limit for $\mathcal{R}$ using $\phi/\pi < 1/2$ [42]. We compare exact simulations to a mean-field approach as explained in Sec. II D; see Fig. 9. Both exact and approximate treatments satisfy the relations (16) when the vertical mirror symmetry is preserved. However, the Hartree approach is unreliable as it predicts incorrect magnitudes for $\mathcal{R}$. Similarly, in the absence of mirror symmetries, exact and approximate tools demonstrate the violation of Eq. (16), but the Hartree approach overestimates the magnitude of $\mathcal{R}$.

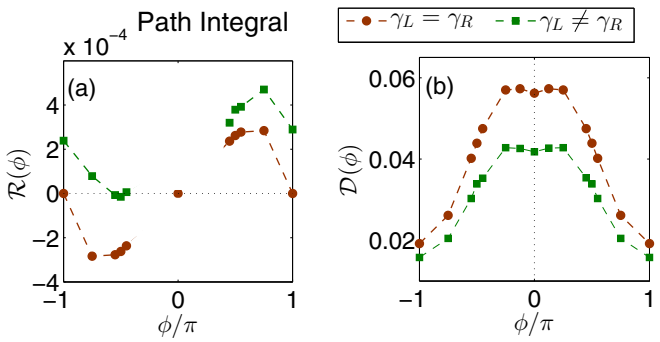

FIG. 8. (Color online) Steady-state behavior of model I with INFPI simulations using nondegenerate dots, $\epsilon_1 = 0.1$, $\epsilon_2 = 0.2$. Setups with a vertical mirror symmetry, $\gamma_{v,n} = 0.1$ (○), and missing mirror symmetries, $\gamma_{L,n} = 0.2$ and $\gamma_{R,n} = 0.05$ (□). Other parameters are $\Delta\mu = 0.6$, $U = 0.1$, $\beta = 50$, $N_s = 6$, and $\delta t = 0.6$.

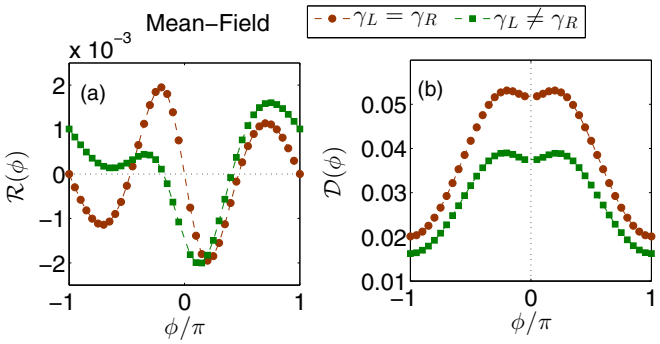

FIG. 9. (Color online) Steady-state behavior of model I using a mean-field scheme, and the same parameters as in Fig. 8. Setups with a vertical mirror symmetry, $\gamma_{v,n} = 0.1$ (○), and missing mirror symmetries, $\gamma_{L,n} = 0.2$ and $\gamma_{R,n} = 0.05$ (□).

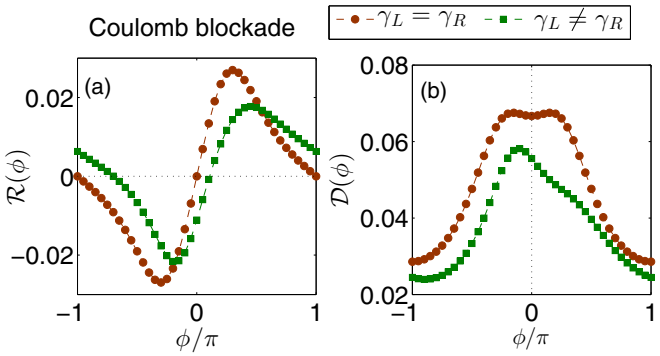

FIG. 10. (Color online) Steady-state behavior of model I in the Coulomb blockade regime with the parameters of Fig. 8 using Eq. (18). Setups with a vertical mirror symmetry, $\gamma_{v,n} = 0.1$ (○), and missing mirror symmetries, $\gamma_{L,n} = 0.2$ and $\gamma_{R,n} = 0.05$ (□).

Previous studies of nonlinear transport in quantum dot systems had indicated that Hartree MF approximation suffers from fundamental artifacts; e.g., it predicts an incorrect hysteresis behavior in the single-impurity Anderson model [41]. Here we find that the method conserves correct transport symmetries, but it produces incorrect values for the nonlinear terms. We have also implemented a Hartree-Fock (HF) approach as described in Ref. [43] by further correcting off-diagonal elements in the Green's function with the expectation values of the coherences $\sigma_{1,2}$. This had reduced the amplitude of the oscillatory pattern around $\phi/\pi = \pm 0.2$, but HF results still overestimate $\mathcal{R}$ by almost an order of magnitude, for $\phi \sim \pi/2$. It is interesting to adopt an equations-of-motion treatment [44] and explore these deviations maintaining higher-order correlation effects.

Complementing Green's function approaches, one can derive a Bloch-type number-resolved master equation for the reduced density matrix using a technique developed by Gurvitz *et al.* [45]. This treatment is valid in the large-bias limit $\Delta\mu \gg \gamma_{v,n}, \Delta\epsilon, T$, with $\Delta\epsilon = \epsilon_1 - \epsilon_2$. In the Coulomb blockade case, $\epsilon_n + U \gg \Delta\mu$, equations of motion for the reduced density matrix are included in Ref. [46], to provide the steady-state current

$$I(\phi) = I_0 \frac{\Delta\epsilon^2}{\Delta\epsilon^2 + I_0\left(2\gamma_R \sin^2\frac{\phi}{2} - \Delta\epsilon\sin\phi\right)}. \qquad (18)$$

Here $I_0 = \frac{2\gamma_L\gamma_R}{2\gamma_L+\gamma_R}$ is the current in the absence of the magnetic field. This expression was derived under the assumption of a unidirectional current, allowing electrons to flow only from the left terminal to the right one. For noninteracting electrons the infinite bias limit can be well approximated by a system with a finite bias, if the electronic levels are placed deep inside the bias window, $\mu_L - \mu_R \gg \epsilon_{1,2}$ [45]. Our parameters satisfy this condition. Equation (18) discloses that the current is oscillatory with ϕ when $\Delta\epsilon \neq 0$, but it shows an asymmetric behavior. This again demonstrates that Onsager relation is violated for interacting systems at finite voltage bias. A peculiar nonanalytic (in ϕ) behavior develops when $\Delta\epsilon \to 0$ as was discussed in Ref. [46].

We now use Eq. (18) and calculate $\mathcal{R}(\phi)$ and $\mathcal{D}(\phi)$, by considering the reversed polarity with $\mu_R \gg \mu_L$. Results are displayed in Fig. 10. It is extremely interesting to note that this infinite-U case shares qualitative similarities with finite-U results, $U/\Delta\mu \sim 0.2$, of Fig. 8 (exact) and Fig. 9 (mean field). Of course, given the underlying large-bias assumption in Eq. (18) the $\mathcal{R}$ and $\mathcal{D}$ components in Fig. 10 are comparable in magnitude. Furthermore, when the vertical mirror symmetry is violated, the even symmetry of $\mathcal{D}$ is clearly broken, given the dominance of high-order conductance terms such as G_3, $G_5, \ldots$ over the linear response term G_1.

We conclude the following: (i) The AB interferometer can act as a charge diode ($\mathcal{R} \neq 0$) in a spatially symmetric device ($\gamma_{v,n}$ are all identical) if the following conditions are simultaneously met: the dots' energies are nondegenerate, the magnetic flux is nonzero $\phi \neq \pi m$, and many-body interactions are in play; see Fig. 8(a). This observation agrees with recent simulations based on wave-packet propagation [47]. (ii) The Hartree mean-field approach properly describes the development of transport symmetries when the device acquires vertical

or horizontal mirror symmetries; its quantitative predictions are unreliable. (iii) The large voltage-bias Coulomb blockade case exhibits similar features to intermediate-bias finite-U simulations. This observation reveals that G_{2n} conductance terms within $\mathcal{R}$ apparently attain a similar functional form with ϕ and U.

B. Model II

Here we simulate with INFPI the dynamics of model II, an AB interferometer coupled to a dissipative environment. The FE provides a mechanism for elastic and inelastic scattering of electrons on dot 1, and it dissipates energy from the AB unit. We focus on an equilibrium environment, $\mu_+ = \mu_-$; in Fig. 15 we further address the role of a nonequilibrium FE on transport symmetries within the AB interferometer. It should be noted that with dot 1 coupled to the FE, the model lacks a horizontal mirror symmetry by construction.

Model II with an equilibrium FE may be mimicked by a noninteracting model with dot 1 connected to a voltage probe. The voltage probe is a metal terminal; its parameters are set so as the net charge current directed towards it, from the AB systems, vanishes. It provides a mechanism for implementing dissipative inelastic scattering of electrons in the interferometer, while allowing one to work in the Landauer formalism of noninteracting electrons. In Ref. [23] we used this machinery and proved that in systems with a vertical mirror symmetry even and odd conductance components of the charge current (14) and (15) obey in steady state the relations (16). When spatial asymmetry in the form $\gamma_L = \gamma_{L,1} = \gamma_{L,2} \neq \gamma_R = \gamma_{R,1} = \gamma_{R,2}$ is introduced, the relations (16) are violated [23]. Here we complement the probe analysis and explore model II with genuine many-body effects: We confirm the relations (16) under a vertical mirror symmetry, study violations of this equation in general cases, and point out that under certain conditions the diode effect, missing in the phenomenological probe treatment, shows up in exact simulations.

In Fig. 11 we display the charge current in the interferometer, either isolated ($U = 0$) or coupled to a FE ($U = 0.1$). We confirm that the former, a coherent system, obeys phase rigidity $I(t,\phi) = I(t,-\phi)$. When the AB setup is coupled to the FE, the transient current and the steady-state value do not transparently expose any symmetry, but Figs. 11(b) and 11(c) demonstrate that in a geometrically symmetric setup, $\gamma_L = \gamma_R$, the symmetries (16) are satisfied in the transient regime and in the steady-state limit.

It is important to recall that the occupations of the dots in the AB interferometer do not satisfy analogous symmetries, even in the isolated $U = 0$ limit. In Fig. 12 we display the occupation of dot 1 and show that, in agreement with analytical results [25], $\sigma_{1,1}(t,\phi)$ does not satisfy a phase symmetry away from the symmetric point. Note that at short time, $\gamma_v t \lesssim 0.5$, the current and the occupation of dot 1 are insensitive to both interactions and the magnetic phase. When U is turned on, the case with $\phi = \pi/2$ approaches steady state significantly faster than the opposite $\phi = -\pi/2$ situation. This is reflected in both the occupation dynamics and the current.

In Fig. 13 we present steady-state data for $\mathcal{R}$ and $\mathcal{D}$. We demonstrate the validity of Eq. (16) in junctions with a vertical mirror symmetry, and its violation in general situations. Note that $\mathcal{D}(\phi) \neq \mathcal{D}(-\phi)$ under a spatial asymmetry, but deviations

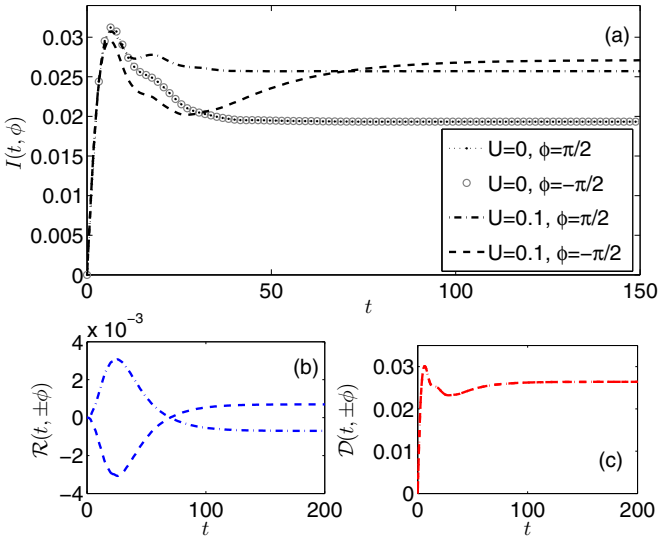

FIG. 11. (Color online) Model II, an interferometer coupled to an equilibrium FE, with a vertical mirror symmetry. (a) Charge current in the AB interferometer, $U = 0$ with $\phi = \pm\pi/2$ (dot and circles, overlapping) and $U = 0.1$ with $\phi = \pi/2$ (dashed-dotted), $\phi = -\pi/2$ (dashed). (b) and (c) Odd and even conductance terms obey the symmetries (16). The quantum dots in the AB interferometer are set at $\epsilon_{1,2} = 0.15$, $\gamma_{v,n} = 0.05$. The FE is set at equilibrium ($\mu_\pm = 0$) with $\epsilon_p = -0.5$ and $\gamma_\pm = 0.2$. The four reservoirs are prepared at the temperature $1/\beta = 50$. Numerical parameters are $\delta t = 0.6$, $N_s = 4$, and $L_s = 120$.

are small, for example $\mathcal{D}(\pi/2) - \mathcal{D}(-\pi/2) \sim 1.5 \times 10^{-4}$. We compare these results to the probe technique as described in Ref. [23]. The coupling of dot 1 to the probe (hybridization strength γ_p) does not directly correspond to the capacitive coupling U thus we can only make a qualitative comparison here. Results are displayed in Fig. 14. Note that we used here a higher electronic temperature, $1/\beta = 25$, to facilitate convergence. It was shown in Ref. [23] that an increase of the metals' temperature only leads to a weaker visibility of the current with the magnetic flux, but it does not alter the oscillation of the current with flux.

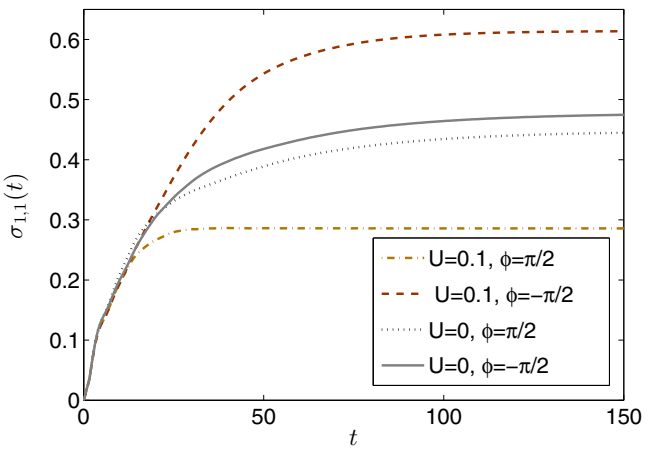

FIG. 12. (Color online) Occupation of dot 1 in a system with a vertical mirror symmetry using the parameters of Fig. 11, $N_s = 3$, $\delta t = 0.8$.

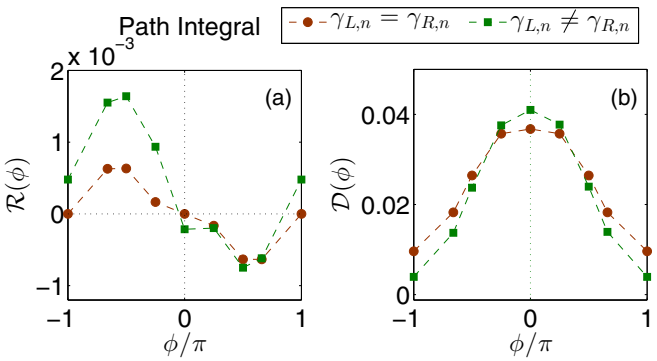

FIG. 13. (Color online) Steady-state values of $\mathcal{R}$ and $\mathcal{D}$ in model II, symmetric $\gamma_{v,n} = 0.2$ (○), and asymmetric $\gamma_{L,n} = 0.05 \neq \gamma_{R,n} = 0.2$ (□) setups. Other parameters are the same as in Fig. 11.

Comparing Fig. 13 (INFPI) to Fig. 14 (probe), we observe that the probe technique provides qualitative correct features. However, in asymmetric setups it brings $\mathcal{R}(\phi = 0) = 0$, even if the dots are nondegenerate [23]. In contrast, INFPI yields a nonzero value for $\mathcal{R}(\phi = 0)$; see Fig. 13. This disagreement has an important implication: The phenomenological probe approach predicts that in the absence of a magnetic flux the AB system cannot act as a diode, though an asymmetry is introduced and (effective) many-body interactions are playing a role. In contrast, INFPI simulations show that the system can act as a diode at zero flux if $\gamma_L \neq \gamma_R$. The fact that the phenomenological probe technique is missing this important functionality (at zero flux) indicates that it does not properly account for electron-electron interactions in the system.

We now explore the role of nonequilibrium effects in the FE, $\Delta\mu_F = \mu_+ - \mu_- \neq 0$. As long as we keep the interferometer biased $\Delta\mu \neq 0$ we recover the symmetries as before, reaching the dynamics as in Fig. 11. Transport symmetries are thus unaffected by the nonequilibrium environment, and this could be justified by noting that in our model dot 1 is coupled to a number operator in the FE, as in Ref. [12], rather than to scattering states [35].

Model II further allows us to explore the development of the "Coulomb drag current" in the interferometer, a result of its coupling to the FE. This effect has important implications in nanoscale electronic junctions: When placing two quantum wires (with independent contacts) into a close proximity, a "drive current" passing through one conductor can induce a "drag current" in the other wire, a result of Coulomb (capacitive) interactions between charges in the two wires; see, e.g., Ref. [48] for an experimental demonstration. In Fig. 15 we explore this effect using INFPI: The interferometer is unbiased, $\Delta\mu = 0$, but we voltage-bias the FE. We show that in a system with a vertical mirror symmetry the drag current is nonzero, an odd function of the magnetic flux. We can drive a positive or a negative current in the AB interferometer; the directionality is induced here through the magnetic flux, not the hybridization coefficients as in other works [49]. Furthermore, by plotting in panel (b) the measure $\mathcal{R} = [I(t,\phi,\Delta\mu_F) + I(t,\phi,-\Delta\mu_F)]/2$ we confirm that the current includes only even powers in $\Delta\mu_F$, missing altogether a linear response term.

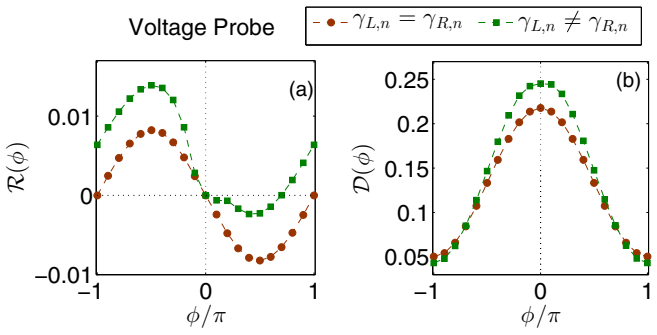

FIG. 14. (Color online) Model II with the FE replaced by a voltage probe coupled to dot 1. The probe equations are detailed in Ref. [23]; symmetric $\gamma_{v,n} = 0.2$ (○), and asymmetric $\gamma_{L,n} = 0.05 \neq \gamma_{R,n} = 0.2$ (□) setups. Parameters are the same as in Figs. 11–13, besides the temperature which is set at $1/\beta = 25$ and $\gamma_p = 0.05$.

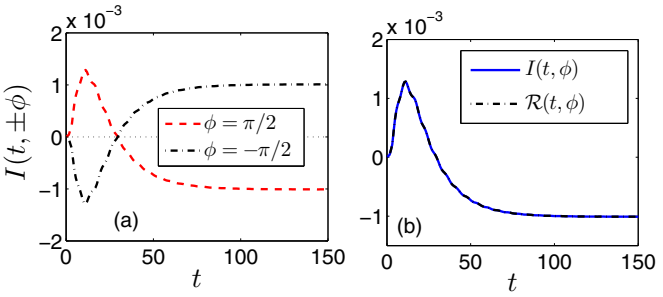

FIG. 15. (Color online) Model II with an out-of-equilibrium FE. (a) A finite drag current is induced in the interferometer (set in equilibrium $\Delta\mu = 0$), a result of its coupling to a nonequilibrium FE with $\Delta\mu_F = 1$. Panel (b) demonstrates that the current in the interferometer is missing a linear response contribution (and all other odd powers of voltage); $\epsilon_{1,2} = 0$, $\gamma_{v,n} = 0.1$, $\gamma_\pm = 0.2$, $\epsilon_p = 0.1$, $U = 0.05$, $\beta = 10$ (facilitating convergence), $\delta t = 0.8$, and $N_s = 3$.

The Coulomb drag effect has been examined so far by breaking the spatial symmetry using uneven contacts, adopting phenomenological rate equations or perturbative treatments; see, e.g., Refs. [49,51,52]. Our work here is a first step towards the exploration of this many-body phenomenon with a broken-time-reversal symmetry, by means of an exact numerical tool.

We summarize our main observations for model II: (i) The relations (16) are satisfied in the transient regime and in the steady-state limit when the vertical mirror symmetry is obeyed. The approach to steady state depends on the magnetic flux. (ii) The probe technique, an effective mean, provides the correct features for $\mathcal{R}$ and $\mathcal{D}$, but it predicts zero dc rectification current in the absence of a magnetic flux, for $\gamma_L \neq \gamma_R$. (iii) The FE may generate a positive or a negative drag current

in an unbiased centrosymmetric AB interferometer, given a nonzero magnetic phase in the system.

IV. SUMMARY

We examined the double-dot AB interferometer with controlled many-body effects, either internal, between electrons on the dots (model I), or between the AB electrons and a dissipative environment (model II). Using a flexible numerically exact tool, we studied the transient and the steady-state characteristics of the charge current in the AB system. We validated magnetic field symmetries of nonlinear transport when the system preserves horizontal or vertical mirror symmetries. Transport asymmetries were displayed and quantified in general geometries. Applications beyond the mean-field level were exemplified, including a charge diode, charge sensing, and the Coulomb drag current.

Earlier studies of magnetotransport properties were limited to steady-state situations, mostly analyzed at the mean-field level. Here, we studied a double-dot AB interferometer with genuine many-body interactions, and we simulated it with a numerically exact tool. The comparison to effective treatments, Hartree MF and the probe technique, reveals that these simplified methods capture correctly transport symmetries, though magnitudes of nonlinear terms may substantially deviate from the exact limit. The study of a limiting case for model I, unidirectional electron current in the Coulomb blockade regime, teaches us that our INFPI results for $\mathcal{R}$ and $\mathcal{D}$, performed at finite interactions $U/\gamma \sim 1$ and bias $\Delta\mu/\gamma = 5$, are qualitatively predictive even for strong interactions $U \to \infty$ and very large bias.

In future studies we plan to examine other many-body models, for example, a nanojunction coupled to internal vibrations. This will be done using INFPI [36] and other perturbative-analytical and numerical schemes such as the Green's function technique [53,54] and quantum master equations [55,56]. Such an analysis would not only resolve transport behavior, but further serve as a critical test for examining the consistency of analytical and numerical truncation schemes [57]. Other ideas involve a detailed analysis of the Coulomb drag effect, harnessing (hot) thermal charge fluctuations to drive a dc current in the interferometer [58]. Finally, we plan to study symmetries of the thermoelectric current using both the phenomenological probe technique and INFPI, with the objective to suggest means for increasing heat-to-work conversion efficiency in nonlinear situations [59–61].

ACKNOWLEDGMENTS

The work of S.B. has been supported by the Early Research Award of D.S., the Martin Moskovits Graduate Scholarship in Science and Technology, and the Lachlan Gilchrist Fellowship Fund. D.S. acknowledges support from the Natural Science and Engineering Research Council of Canada.

[1] L. Onsager, Phys. Rev. **37**, 405 (1931); **38**, 2265 (1931); H. B. G. Casimir, Rev. Mod. Phys. **17**, 343 (1945).
[2] Y. Imry, *Introduction to Mesoscopic Physics*, 2nd ed. (Oxford University Press, Oxford, 2002).
[3] A. Yacoby, M. Heiblum, D. Mahalu, and H. Shtrikman, Phys. Rev. Lett. **74**, 4047 (1995).
[4] H. Linke, W. D. Sheng, A. Svensson, A. Löfgren, L. Christensson, H. Q. Xu, P. Omling, and P. E. Lindelof, Phys. Rev. B **61**, 15914 (2000).
[5] A. Löfgren, C. A. Marlow, I. Shorubalko, R. P. Taylor, P. Omling, L. Samuelson, and H. Linke, Phys. Rev. Lett. **92**, 046803 (2004).
[6] C. A. Marlow, R. P. Taylor, M. Fairbanks, I. Shorubalko, and H. Linke, Phys. Rev. Lett. **96**, 116801 (2006).
[7] J. Wei, M. Shimogawa, Z. Wang, I. Radu, R. Dormaier, and D. H. Cobden, Phys. Rev. Lett. **95**, 256601 (2005).
[8] R. Leturcq, D. Sanchez, G. Götz, T. Ihn, K. Ensslin, D. C. Driscoll, and A. C. Gossard, Phys. Rev. Lett. **96**, 126801 (2006); R. Leturcq, R. Bianchetti, G. Götz, T. Ihn, K. Ensslin, D. C. Driscoll, and A. C. Gossard, Physica E **35**, 327 (2006).
[9] L. Angers, E. Zakka-Bajjani, R. Deblock, S. Gueron, H. Bouchiat, A. Cavanna, U. Gennser, and M. Polianski, Phys. Rev. B **75**, 115309 (2007).
[10] G. M. Gusev, Z. D. Kvon, E. B. Olshanetsky, and A. Y. Plotnikov, Europhys. Lett. **88**, 47007 (2009).
[11] F. G. G. Hernandez, G. M. Gusev, Z. D. Kvon, and J. C. Portal, Phys. Rev. B **84**, 075332 (2011).
[12] K. Saito and Y. Utsumi, Phys. Rev. B **78**, 115429 (2008).
[13] Y. Utsumi and K. Saito, Phys. Rev. B **79**, 235311 (2009).
[14] S. Nakamura, Y. Yamauchi, M. Hashisaka, K. Chida, K. Kobayashi, T. Ono, R. Leturcq, K. Ensslin, K. Saito, Y. Utsumi, and A. C. Gossard, Phys. Rev. Lett. **104**, 080602 (2010).
[15] S. Nakamura, Y. Yamauchi, M. Hashisaka, K. Chida, K. Kobayashi, T. Ono, R. Leturcq, K. Ensslin, K. Saito, Y. Utsumi, and A. C. Gossard, Phys. Rev. B **83**, 155431 (2011).
[16] D. Sanchez and M. Büttiker, Phys. Rev. Lett. **93**, 106802 (2004); Int. J. Quantum Chem. **105**, 906 (2005).
[17] B. Spivak and A. Zyuzin, Phys. Rev. Lett. **93**, 226801 (2004).
[18] A. R. Hernandez and C. H. Lewenkopf, Phys. Rev. Lett. **103**, 166801 (2009).
[19] J. S. Lim, D. Sanchez, and R. Lopez, Phys. Rev. B **81**, 155323 (2010). Note that in this work the current expansion with voltage is written as $I = G_0\Delta\mu + G_1\Delta\mu^2 + \cdots$.
[20] T. Kubo, Y. Ichigo, and Y. Tokura, Phys. Rev. B **83**, 235310 (2011).
[21] V. Puller, Y. Meir, M. Sigrist, K. Ensslin, and T. Ihn, Phys. Rev. B **80**, 035416 (2009).
[22] M. Büttiker, Phys. Rev. B **32**, 1846 (1985); **33**, 3020 (1986); IBM J. Res. Dev. **32**, 63 (1988).
[23] S. Bedkihal, M. Bandyopadhyay, and D. Segal, Phys. Rev. B **88**, 155407 (2013); Europhys J. B **86**, 506 (2013).
[24] D. Segal, A. J. Millis, and D. R. Reichman, Phys. Rev. B **82**, 205323 (2010).
[25] S. Bedkihal, M. Bandyopadhyay, and D. Segal, Phys. Rev. B **87**, 045418 (2013).
[26] D. Segal, A. J. Millis, and D. R. Reichman, Phys. Chem. Chem. Phys. **13**, 14378 (2011).
[27] M. Sindel, A. Silva, Y. Oreg, and J. von Delft, Phys. Rev. B **72**, 125316 (2005).

[28] V. Kashcheyevs, A. Schiller, A. Aharony, and O. Entin-Wohlman, Phys. Rev. B **75**, 115313 (2007).
[29] H. A. Nilsson, O. Karlstrom, M. Larsson, P. Caroff, J. N. Pedersen, L. Samuelson, A. Wacker, L.-E. Wernersson, and H. Q. Xu, Phys. Rev. Lett. **104**, 186804 (2010); O. Karlström, J. N. Pedersen, P. Samuelsson, and A. Wacker, Phys. Rev. B **83**, 205412 (2011).
[30] J. König and Y. Gefen, Phys. Rev. Lett. **86**, 3855 (2001); Phys. Rev. B **65**, 045316 (2002).
[31] M. W.-Y. Tu, W.-M. Zhang, J. Jin, O. Entin-Wohlman, and A. Aharony, Phys. Rev. B **86**, 115453 (2012).
[32] S. Bedkihal and D. Segal, Phys. Rev. B **85**, 155324 (2012).
[33] T. Kubo, Y. Tokura, and S. Tarucha, J. Phys. A: Math. Theor. **43**, 354020 (2010).
[34] D. Sanchez and K. Kang, Phys. Rev. Lett. **100**, 036806 (2008).
[35] V. I. Puller and Y. Meir, Phys. Rev. Lett. **104**, 256801 (2010).
[36] L. Simine and D. Segal, J. Chem. Phys. **138**, 214111 (2013).
[37] J. E. Hirsch, Phys. Rev. B **28**, 4059 (1983).
[38] S. Weiss, R. Hützen, D. Becker, J. Eckel, R. Egger, and M. Thorwart, Phys. Status Solidi B **250**, 2298 (2013).
[39] N. Makri, J. Math. Phys. **36**, 2430 (1995).
[40] A. Komnik and A. O. Gogolin, Phys. Rev. B **69**, 153102 (2004).
[41] B. Horvath, B. Lazarovits, O. Sauret, and G. Zarand, Phys. Rev. B **77**, 113108 (2008).
[42] INFPI simulations allow us to explore the quasi-steady-state regime, limited by the recurrence time which is dictated by the finite discretization of the fermionic baths. Numerical simulations in Fig. 8 are limited to certain phases since the relaxation time towards steady state significantly grows when the magnetic phase is small, $\phi/\pi < 1/2$. Indeed, in Ref. [32] we had shown analytically that the two-dot dynamics is controlled by rate constants of the form $[1 \pm \cos(\phi/2)]$; the rate proportional to $[1 - \cos(\phi/2)]$ apparently controls the dynamics of $\mathcal{R}(t,\phi)$.
[43] M. Goldstein and R. Berkovits, New J. Phys. **9**, 118 (2007).
[44] H. Haug and A.-P. Jauho, *Quantum Kinetics in Transport and Optics of Semiconductors* (Springer, Berlin, 1996).
[45] S. A. Gurvitz and Ya S. Prager, Phys. Rev. B **53**, 15932 (1996); S. A. Gurvitz, *ibid.* **57**, 6602 (1998).
[46] F. Li, X.-Q. Li, W.-M. Zhang, and S. A. Gurvitz, Europhys. Lett. **88**, 37001 (2009).
[47] Y. Li, J. Zhou, F. Marchesoni, and B. Li, Sci. Rep. **4**, 4566 (2014).
[48] D. Laroche, G. Gervais, M. P. Lilly, and J. L. Reno, Nat. Nanotechnol. **6**, 793 (2011).
[49] R. Sanchez, R. Lopez, D. Sanchez, and M. Büttiker, Phys. Rev. Lett. **104**, 076801 (2010).
[50] O. Entin-Wohlman and A. Aharony, Phys. Rev. B **85**, 085401 (2012).
[51] M. C. Goorden and M. Büttiker, Phys. Rev. Lett. **99**, 146801 (2007).
[52] V. Moldoveanu and B. Tanatar, Europhys. Lett. **86**, 67004 (2009).
[53] O. Hod, R. Baer, and E. Rabani, J. Phys. Condens. Matter **20**, 383201 (2008).
[54] D. Rai and M. Galperin, Phys. Rev. B **86**, 045420 (2012).
[55] R. Härtle, G. Cohen, D. R. Reichman, and A. J. Millis, Phys. Rev. B **88**, 235426 (2013).
[56] M. Leijnse and M. R. Wegewijs, Phys. Rev. B **78**, 235424 (2008).
[57] T. J. Levy and E. Rabani, J. Phys.: Condens. Matter **25**, 115302 (2013); J. Chem. Phys. **138**, 164125 (2013).
[58] R. Sanchez and M. Büttiker, Phys. Rev. B **83**, 085428 (2011).
[59] D. Sanchez and R. Lopez, Phys. Rev. Lett. **110**, 026804 (2013).
[60] S.-Y. Hwang, D. Sanchez, M. Lee, and R. Lopez, New J. Phys. **15**, 105012 (2013).
[61] R. S. Whitney, Phys. Rev. Lett. **112**, 130601 (2014).